nature chemistry

ARTICLES

https://doi.org/10.1038/s41557-021-00797-w

Spontaneous N_2 formation by a diruthenium complex enables electrocatalytic and aerobic oxidation of ammonia

Michael J. Trenerry[1,2], Christian M. Wallen[1,2], Tristan R. Brown[1], Sungho V. Park[1] and John F. Berry[1]✉

The electrochemical conversion of ammonia to dinitrogen in a direct ammonia fuel cell (DAFC) is a necessary technology for the realization of a nitrogen economy. Previous efforts to catalyse this reaction with molecular complexes required the addition of exogenous oxidizing reagents or application of potentials greater than the thermodynamic potential for the oxygen reduction reaction—the cathodic process of a DAFC. We report a stable metal–metal bonded diruthenium complex that spontaneously produces dinitrogen from ammonia under ambient conditions. The resulting reduced diruthenium material can be reoxidized with oxygen for subsequent reactions with ammonia, demonstrating its ability to spontaneously promote both half-reactions necessary for a DAFC. The diruthenium complex also acts as a redox mediator for the electrocatalytic oxidation of ammonia to dinitrogen at potentials as low as −255 mV versus $Fc^{0/+}$ and operates below the oxygen reduction reaction potential in alkaline conditions, thus achieving a thermodynamic viability relevant for the future development of DAFCs.

The development of zero-carbon fuel technology is of existential importance to society. The prevailing framework for addressing this issue is the 'hydrogen economy', but due to major practical limitations (for example, production, storage, distribution, safety), alternative zero-carbon fuel economies have been proposed. Most notable among these is the 'nitrogen economy', with a focus on the use of ammonia as a fuel[1–5]. Due to the large-scale production of ammonia through the (still carbon-intensive) Haber–Bosch process, extensive national and global infrastructures dedicated to the mass distribution and storage of ammonia are already in place[1,3,5,6]. Moreover, ammonia's reduced explosion hazard and superior compressibility at mild pressures present important advantages over hydrogen in terms of safety and efficiency, and the use of ammonia as a fuel is already being considered, especially for maritime transportation[7]. Furthermore, a proposed functional nitrogen/ammonia economy[2–5,8] can be established through the continued development of two key technologies: the synthesis of 'green' ammonia from nitrogen and water powered by renewable sources[6,9–11], and the efficient oxidation of ammonia to power fuel cells (Fig. 1a)[3,5,12,13].

The primary challenge in developing direct ammonia fuel cells (DAFCs) lies in identifying electrocatalysts for the ammonia oxidation reaction (AOR). Moreover, a practical fuel cell requires coupling of the AOR at the anode to the oxygen reduction reaction (ORR) at the cathode[5,8]. For an AOR catalyst to be viable in DAFCs, two requirements must be met: for thermodynamic viability, the operating potential of the catalyst must lie below the thermodynamic ORR potential, while kinetic viability involves overcoming resistive losses with useful rates of reactivity. Intensive recent efforts in the field of inorganic chemistry have led to the discovery of several new AOR catalysts[14–20]. In the known systems that report electrocatalysis, however, the operating potentials for electrocatalytic AOR either exceed the upper bound dictated by ORR or transcend it by only a small margin (<50 mV). The shortcomings of these systems may be attributed in part to the mechanisms through which AOR is catalysed. Specifically, known monometallic ruthenium catalysts invoke highly oxidized imido and nitrido intermediates, which necessitate high operating potentials[14,15].

We now report a metal–metal bonded diruthenium mixed-valent ($[Ru_2]^{5+}$) complex, $Ru_2(chp)_4OTf$ (**2**, $chp^- = 6$-chloro-2-hydroxypyridinate), that spontaneously forms nitrogen from ammonia without any applied potential and mediates electrocatalytic oxidation of ammonia at −255 mV versus $Fc^{0/+}$ (Fig. 1b). Moreover, we have found that $[Ru_2]^{5+}$ species capable of promoting spontaneous ammonia oxidation can be regenerated in batch cycles from the $[Ru_2]^{4+}$ reaction products of **2** and ammonia by using oxygen as the terminal oxidant, demonstrating chemically these complexes' ability to promote both of the DAFC half-reactions. Mechanistic and computational insights indicate that the metal–metal bonds in **2** and related compounds impart unique chemical reactivity that enables electrocatalytic oxidation of ammonia at low overpotentials and avoids the high oxidation state intermediates accessed in monometallic ruthenium catalysts.

Results and discussion

Defining the thermodynamic DAFC viability zone. A general DAFC design is depicted in Fig. 1a (left), where the ORR and mediated AOR occur as the cathodic and anodic half-reactions, respectively. These transformations and the net fuel cell reaction are outlined in equations (1)–(3) with potentials referenced to the $Fc^{0/+}$ redox couple in CH_3CN (NRR is the nitrogen reduction reaction)[21]. Proton equivalents in NRR and ORR processes are balanced using the solvated NH_4^+/NH_3 conjugate acid–base pair

[1]Department of Chemistry, University of Wisconsin-Madison, Madison, WI, USA. [2]These authors contributed equally: Michael J. Trenerry, Christian M. Wallen. ✉e-mail: berry@chem.wisc.edu

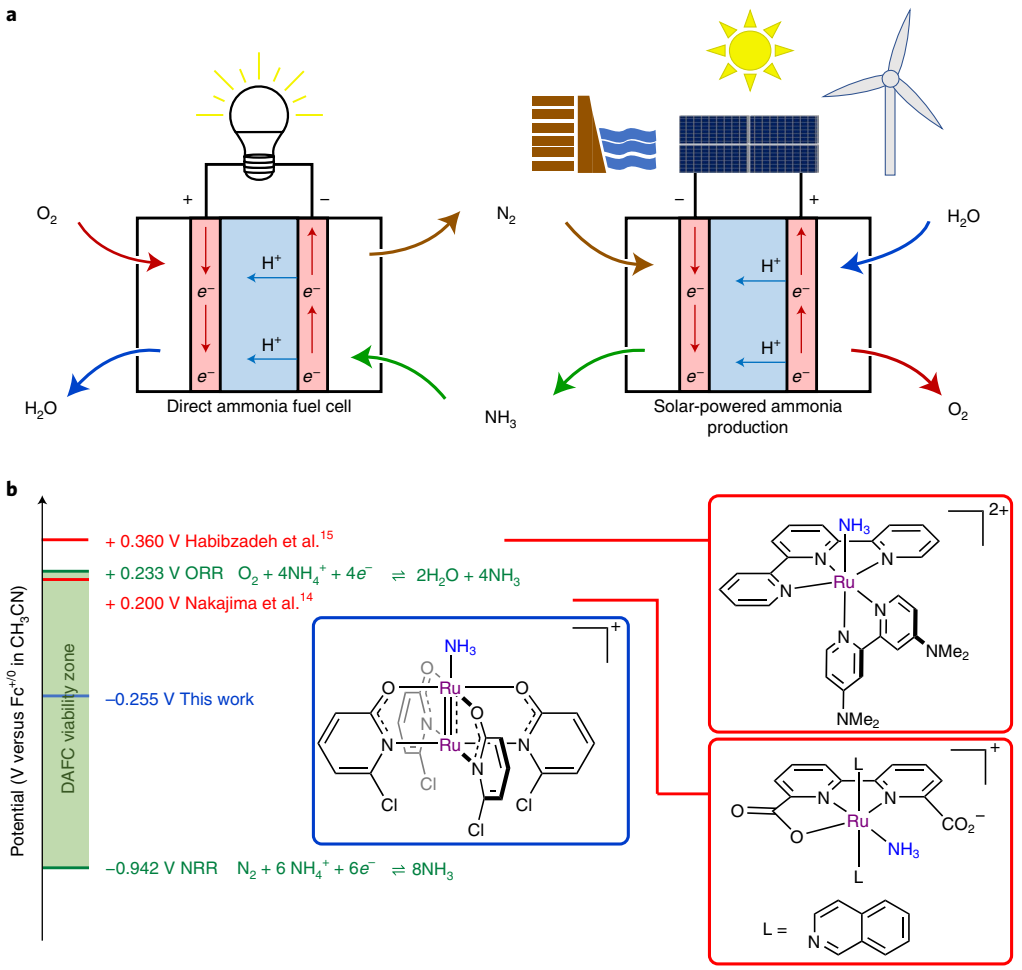

Fig. 1 | Overview of a nitrogen/ammonia fuel economy and progress towards catalysed DAFCs. a, The essential components of a nitrogen/ammonia economy. Right: electrochemical ammonia synthesis from air and water. Left: DAFC. **b**, The operating potentials for previous ruthenium-based molecular AOR catalysts are shown in red, with the operating potential for $Ru_2(chp)_4NH_3^+$ (formed from reaction of **2** and NH_3) shown in blue. There are also iron catalysts that operate at 0.7 V (ref. [18]) and 0.45 V (ref. [20]) versus $Fc^{0/+}$. Potentials for E°_{NRR} (ref. [22]) and E°_{ORR} (ref. [23]), shown in green, are defined under the assumption of a buffered system with 1:1 $[NH_4^+]$:$[NH_3]$ at 1 M concentrations in CH_3CN, using a pK_a value of 16.5 for NH_4^+ in CH_3CN (ref. [24]).

with corresponding potentials E°_{NRR} (ref. [22]) and E°_{ORR} (ref. [23]) calculated according to the literature-reported pK_a value for NH_4^+ in CH_3CN (ref. [24]).

NRR :

$$N_{2(g)} + 6\,NH^+_{4(CH_3CN)} + 6\,e^- \rightleftharpoons 8\,NH_{3(CH_3CN)} \quad (1)$$

$$E^\circ_{NRR} = -0.942\ V\ (AOR\ at\ E_{op})$$

ORR :

$$O_{2(g)} + 4\,NH^+_{4(CH_3CN)} + 4e^- \rightleftharpoons 2H_2O_{(CH_3CN)} + 4NH_{3(CH_3CN)} \quad (2)$$

$$E^\circ_{ORR} = 0.233\ V$$

Net :

$$4NH_{3(CH_3CN)} + 3O_{2(g)} \rightleftharpoons 2N_{2(g)} + 6H_2O_{(CH_3CN)} \quad (3)$$

$$E_{cell} = E^\circ_{ORR} - E_{op}$$

$$E_{cell} > 0\ only\ if\ E_{op} < E^\circ_{ORR}$$

Ammonia oxidation is a difficult, six-electron half-reaction and must be catalysed to achieve efficient conversion. Electrocatalytic AOR therefore requires an oxidative overpotential, η, relative to E°_{NRR}, such that the AOR operating potential, E_{op}, is defined as $E^\circ_{NRR} + \eta$. A basic thermodynamic analysis indicates that E_{op} must be less than E°_{ORR} in order for the DAFC to produce energy (that is, achieve E_{cell} greater than zero). The thermodynamic reduction potentials for the NRR and ORR half-reactions thus respectively define the lower and upper bounds of a thermodynamic 'DAFC viability zone' inside which the AOR must be mediated to achieve a productive fuel cell (Fig. 1b). Several research groups have searched intensively for molecular catalysts that can operate within this range of potentials[14–20]. The operating potential for our electrocatalyst is 455 mV lower than what has been previously reported among other molecular ruthenium electrocatalysts[14,15], thus falling substantially deeper within the thermodynamic DAFC viability zone.

To evaluate AOR catalysts operating in organic solvents, we consider E°_{NRR} and E°_{ORR} relative to the $Fc^{0/+}$ redox couple in CH_3CN. It is important to recognize that these potentials are typically studied under aqueous conditions versus the normal hydrogen electrode, and that conversions to non-aqueous media are not straightforward (further details on referencing are given in the

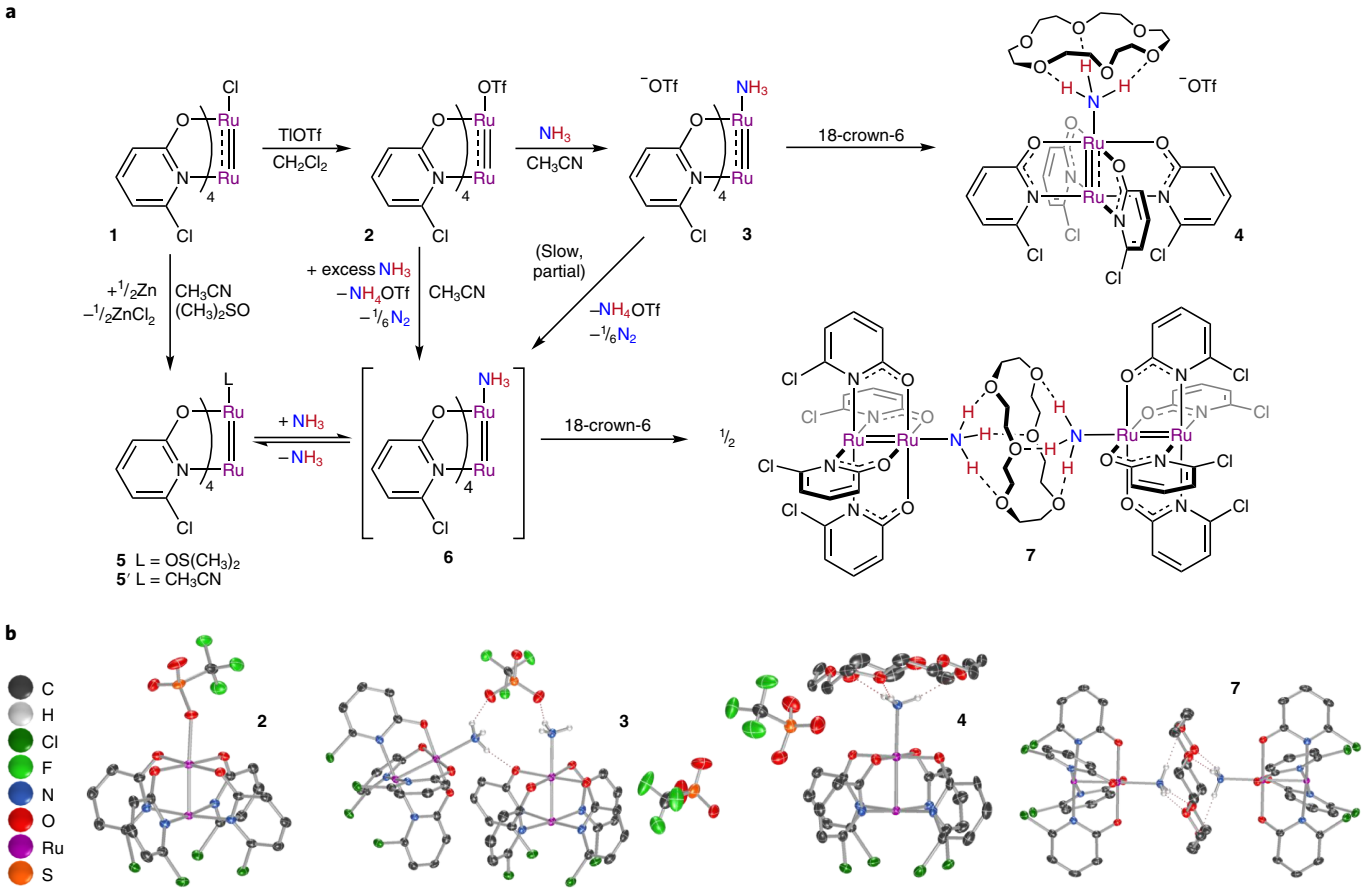

Fig. 2 | Synthesis and structural characterization of key Ru_2 compounds. a, Synthesis and reactivity of diruthenium compounds. **b**, Crystal structures of compounds **2**, **3**, **4** and **7**. Thermal ellipsoids are depicted at 50% probability. All hydrogen atoms bound to carbon are omitted for simplicity.

Supplementary Information). This leads to several alternative ways of defining the thermodynamic DAFC viability zone (Supplementary Table 14 and Supplementary Fig. 9). To address the somewhat ambiguous definition of the DAFC potentials in non-aqueous media, we have investigated the chemical redox reaction between oxygen and the reduced $[Ru_2]^{4+}$ form of our electrocatalyst, observing facile reoxidation to the catalytically active $[Ru_2]^{5+}$ form. This reactivity confirms that, despite referencing ambiguities, our system operates within the thermodynamic DAFC viability zone.

Synthesis and reactivity of diruthenium compounds. Our research group has focused on the ability of *d*-orbital interactions in metal–metal bonded compounds to facilitate multielectron reactions[25–28]. Recently, we have explored the chemistry of paramagnetic Ru_2 compounds supported by chp^- equatorial ligands, as shown in Fig. 2. These ligands support air-stable, purple $[Ru_2]^{5+}$ compounds (Ru–Ru bond order, 2.5)[25,29–31] that may be chemically reduced to the Ru=Ru doubly bonded $[Ru_2]^{4+}$ oxidation state, yielding brown, air-sensitive compounds[32,33].

The new purple complex $Ru_2(chp)_4OTf$ (**2**) was prepared by metathesis of $Ru_2(chp)_4Cl$ (**1**) with TlOTf (Fig. 2a). Addition of 1 equivalent of NH_3 to **2** at −25 °C yields $[Ru_2(chp)_4NH_3]OTf$ (**3**). Both **2** and **3** have been crystallographically characterized (Fig. 2b). The intermolecular hydrogen-bonding interactions in the crystal structure of **3** can be tamed upon exposure to 18-crown-6 (18-c-6) at −25 °C to yield $[Ru_2(chp)_4(NH_3)(18\text{-c-}6)]OTf$ (**4**). The structure of **4** shown in Fig. 2b reveals that all three hydrogen atoms on the NH_3 ligand are hydrogen bonded to oxygen atoms in 18-c-6 (N···O distances range from 3.03 to 3.05 Å for the major disordered component).

At room temperature, solutions of **3** are unstable and slowly produce an amber-coloured species, suggesting reduction to the $[Ru_2]^{4+}$ oxidation state. Stirring **2** with excess ammonia results in immediate formation of **3**, followed by a much slower reduction to an amber-coloured $[Ru_2]^{4+}$ species, with the reaction typically completed overnight. Characterization of these amber-coloured solutions with electronic absorption and ^{1}H-NMR spectroscopy (Supplementary Fig. 11 and Extended Data Fig. 1) suggests the presence of two $[Ru_2]^{4+}$ species in equilibrium: $Ru_2(chp)_4(NH_3)$ (**6**) and $Ru_2(chp)_4(NCCH_3)$ (**5'**, Fig. 2a). This assignment is further supported by spectroscopic data collected on solutions in which ammonia has been added to $Ru_2(chp)_4$–$OS(CH_3)_2$ (**5**), a $[Ru_2]^{4+}$ complex with a labile dimethylsulfoxide (DMSO) solvent molecule in the axial position formed by zinc reduction of **1** in DMSO[33]. It was possible to grow crystals of **6** from these solutions and the X-ray data establish the proposed molecular connectivity but do not lead to a stable structural refinement. To provide structural evidence for the binding of NH_3 to the Ru_2 core, addition of 18-c-6 to a solution containing **6** yields $[Ru_2(chp)_4(NH_3)]_2(18\text{-c-}6)$ (**7**), which was isolated and structurally characterized. This complex is structurally similar to the $[Ru_2]^{5+}$ complex **4**, but here 18-c-6 engages in six hydrogen bonds (N···O distances range from 3.06 to 3.22 Å) bringing together two $[Ru_2]^{4+}$ ammine complexes.

Reduction of **2** to the $[Ru_2]^{4+}$ oxidation state solely by addition of ammonia suggested that ammonia was being oxidized. To test for the formation of the likely oxidation product, N_2, **2** was subjected to excess $^{15}NH_3$ in an argon atmosphere and $^{15}N^{15}N$ was detected in the

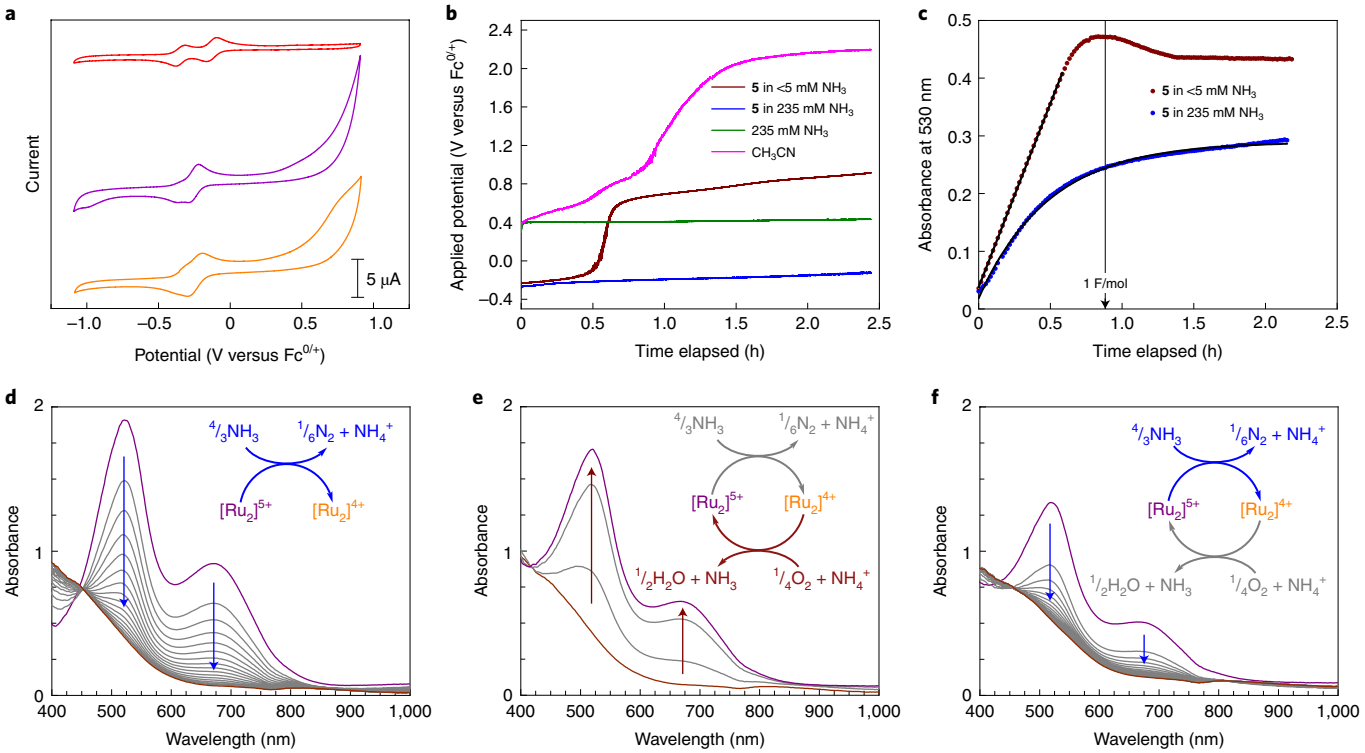

Fig. 3 | Electrochemical and spectroscopic investigations of Ru_2-catalysed ammonia oxidation. a, Cyclic voltammograms collected at 100 mV s^{-1} in CH_3CN using a glassy carbon disk electrode and 100 mM Bu_4NPF_6 as the supporting electrolyte. From top to bottom are cyclic voltammograms of **2** in equilibrium with **5′**$^{+}$ (red trace), **3** formed from the addition of 3.2 molar equivalents of NH_3 to **2** (purple trace), and **6** formed from the addition of 10 molar equivalents of NH_3 to **5** (orange trace). **b**, Controlled current (0.5 mA) traces for electrochemical oxidation of **5** (0.22 mM) with <5 mM (red trace) or 235 mM NH_3 (blue trace) in CH_3CN. Control experiments are also shown: 235 mM NH_3 with no $[Ru_2]$ (green trace), and solution with no NH_3 and no $[Ru_2]$ (pink trace). Electrolyses were performed using an RVC block working electrode and 100 mM Bu_4NPF_6 as the supporting electrolyte. **c**, Absorbance at 530 nm during controlled current bulk electrolysis of **5** with <5 mM (red trace) or 235 mM NH_3 (blue trace) in CH_3CN. Fit parameters are shown in Supplementary Table 17. **d**–**f**, Electronic absorption spectra monitoring reduction of **2** with 100 equivalents of NH_3 (**d**), the subsequent reoxidation with oxygen (**e**) and re-reduction with an additional 100 equivalents of NH_3 (**f**). Time intervals between scans are 5 min.

headspace in 40% yield via calibrated mass spectrometry analysis. This yield is based on a 6:1 molar ratio between **2** and N_2 (equation (4)). Remarkably, we have also observed a $^{15}N^{15}N$ yield of 12% when using aqueous $^{15}NH_3$, demonstrating that water hinders ammonia oxidation by **2** but does not shut down the reaction entirely. Since **2** contains a $[Ru_2]^{5+}$ core, a one-electron oxidized form of the $[Ru_2]^{4+}$ core in **6**, we explored the electrochemical features of **2** to see whether an electrocatalytic cycle for the AOR could be developed on the basis of these stoichiometric studies.

$$6\,Ru_2(chp)_4OTf\,(2) + 14\,NH_3 \rightarrow N_2 + 6\,Ru_2(chp)_4(NH_3)\,(6) + 6\,NH_4OTf \quad (4)$$

Electrochemistry of diruthenium ammine complexes. The cyclic voltammogram of **2** in CH_3CN (Fig. 3a, red trace) showed reversible events at $E_{1/2} = -347$ mV and −128 mV versus $Fc^{0/+}$, respectively assigned to the $[Ru_2]^{4+/5+}$ redox couples for **2** and the solvent complex $[Ru_2(chp)_4\text{–}NCCH_3]^+$ (that is, **5′**$^{+}$) which exist in equilibrium in solution. The addition of 0.8 equivalents of ammonia created a new reversible feature at $E_{1/2} = -255$ mV, which grew with additional ammonia equivalents, while eliminating the waves assigned to the $[Ru_2]^{4+/5+}$ couples of **2** and **5′**$^{+}$ (Fig. 3a, purple trace). This new feature is assigned to the $[Ru_2]^{4+/5+}$ redox couple for the $[Ru_2(chp)_4(NH_3)]^+$ cation in **3** (that is, **6**$^{+}$), which is confirmed by its appearance in voltammograms collected for **5** in the presence of ammonia (Fig. 3a, yellow trace). Peak currents further increased and saturated at higher concentrations of ammonia while retaining a waveform indicative of diffusion-controlled kinetics (Supplementary Fig. 15). This behaviour is consistent with an 'electrocatalytic' mechanism in which fast electron transfer is followed by a slow rate of reaction with ammonia, and we turned to bulk electrolysis techniques to study this electrocatalytic reactivity in further detail.

Controlled current coulometry (CCC, Fig. 3b) was performed to probe for an electrocatalytic AOR promoted by diruthenium species, and electronic absorption spectra were simultaneously collected throughout each CCC experiment (Supplementary Fig. 12). A schematic of the spectroelectrochemical cell used and an outline of processes occurring during electrolysis are given in Extended Data Figs. 2 and 3, respectively. Starting from the insoluble Ru_2 complex **5**, two different sets of reaction conditions were examined. With the addition of minimal NH_3 necessary to dissolve solid **5** (0.22 mM $[Ru_2]$ and <5 mM $[NH_3]$, Fig. 3b, red trace), 0.5 mA current was initially passed at −245 mV, approximately the $E_{1/2}$ of **6**, but the applied electrode potential rapidly started to increase after 36 min (1.08 C charge passed, 0.68e^- equivalents versus $[Ru_2]$) to values exceeding 600 mV. The abrupt shift to higher applied potentials marks a transition from oxidation of the initial $[Ru_2]^{4+}$ species to a different predominant electrode process, probably indicating depletion of **6** at the reticulated vitreous carbon (RVC) electrode surface and formation of **6**$^{+}$. Electronic absorption data (Fig. 3c, red trace) support this interpretation and show charge-dependent

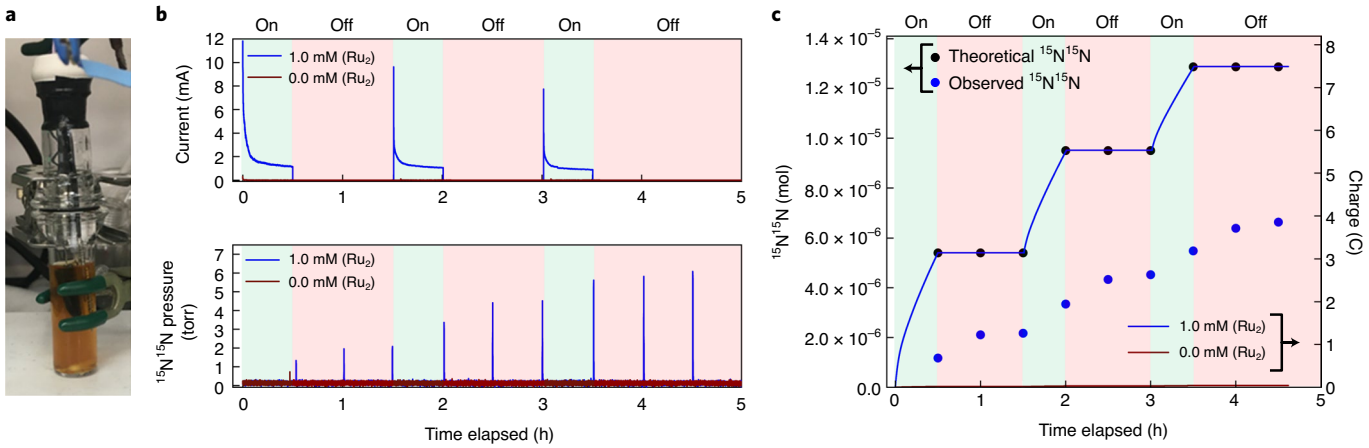

Fig. 4 | Equipment used and data collected in Faradic efficiency experiments. a, Bulk electrolysis cell used in Faradaic efficiency experiments. **b**, Current traces (top) and $m/z = 30$ mass spectrometry traces (bottom) collected for cycled bulk electrolysis of solutions containing Ru_2 species, Bu_4NPF_6 electrolyte and $^{15}NH_3$ (blue trace), and solutions containing only Bu_4NPF_6 electrolyte and $^{15}NH_3$ (red trace). **c**, Left axis: theoretical (black) and observed (blue) yields of $^{15}N^{15}N$ produced by the reaction of Ru_2 species with $^{15}NH_3$. Right axis: charge passed during cycled bulk electrolysis of solutions containing Ru_2 species, Bu_4NPF_6 electrolyte and $^{15}NH_3$ (blue trace), and solutions containing only Bu_4NPF_6 electrolyte and $^{15}NH_3$ (red trace).

linear increases in characteristic $[Ru_2]^{5+}$ absorbance features at 530 and 675 nm. Absorbance values plateaued after the passage of one charge equivalent with respect to **5** (Fig. 3c, 1 F mol^{-1}), indicating stoichiometric conversion from $[Ru_2]^{4+}$ to $[Ru_2]^{5+}$ species, respectively amber and purple in colour. Introduction of excess $^{15}NH_3$ to the reaction mixture after electrolysis afforded the colour change from purple to amber, also seen in the reaction of **2** with ammonia, indicating reduction back to the $[Ru_2]^{4+}$ oxidation state. Additionally, $^{15}N^{15}N$ was detected in the headspace by mass spectrometry, confirming that N_2 is formed from the oxidation of ammonia as part of this transformation.

A second CCC experiment was then performed where **5** was treated with 1,070 equivalents excess of ammonia (Fig. 3b, blue trace), during which 0.5 mA current was sustained for 2.5 h (4.40 C charge passed, or 2.8e^- equivalents versus $[Ru_2]$) at applied potentials ranging from −284 to −121 mV and with no increase to potentials capable of oxidizing ammonia directly at the RVC electrode surface (~400 mV, Fig. 3b, green trace). Electrolysis of $[Ru_2]^{4+}$ species thus remained the predominant electrode process well beyond the passage of stoichiometric charge required for complete one-electron oxidation of **6** (1.6 C). This implies that exogenous ammonia continually reduces $\mathbf{6}^+$ formed electrochemically over the course of the experiment, thereby regenerating **6** and delaying the full conversion to $[Ru_2]^{5+}$ products. Concomitant electronic absorption data (Fig. 3c, blue trace) confirm this hypothesis, showing a diminished net rate of $[Ru_2]^{5+}$ formation relative to the otherwise identical CCC experiment performed at a lower concentration of ammonia. Modelling of these data indicates first-order kinetics in $[Ru_2]^{5+}$ for the rate-determining ammonia oxidation step ($k_{obs} = 5.63 \times 10^{-4}$ s^{-1} at 235 mM NH_3 at room temperature).

Controlled potential coulometry (CPC) experiments using $^{15}NH_3$ were performed to determine the Faradaic efficiency of electrocatalytic ammonia oxidation. After a sequence of three 30 min exposures of solutions of **2** in 640 mM $^{15}NH_3$ to an applied potential of 0.00 V versus $Fc^{0/+}$, quantitative headspace analysis for $^{15}N^{15}N$ indicated a lower bound of 52% Faradaic efficiency and five turnovers (Fig. 4). No $^{15}N^{15}N$ was observed in an otherwise identical CPC experiment performed in the absence of **2**. The sustained passage of superstoichiometric charge at potentials near the $[Ru_2]^{4+/5+}$ redox couple in CCC experiments and the direct observation of catalytic $^{15}N^{15}N$ formation in CPC experiments demonstrate $\mathbf{6}^+$ to be an effective AOR electrocatalyst. This system also displays surprising longevity of electrocatalytic activity, as CCC was performed continuously for 2.5 h at potentials well under those required to oxidize ammonia in the absence of diruthenium complex, and CPC experiments showed no indication of catalyst arrest over 4.5 h.

Reoxidation of $[Ru_2]^{4+}$ species with oxygen. Our electrochemical experiments demonstrated spontaneous formation of N_2 from the reaction of NH_3 with $[Ru_2]^{5+}$ species and suggested the accessibility of the $[Ru_2]^{4+/5+}$ redox couple at potentials lower than the thermodynamic ORR potential. Given the ambiguity of defining the latter value in organic solvents, however, we next sought to explore chemical reoxidation of $[Ru_2]^{4+}$ species through direct reaction with O_2. Addition of 100 equivalents of NH_3 to **2** in CH_3CN at room temperature results in the immediate formation of **3** followed by slow reduction to $[Ru_2]^{4+}$ over 1.5 h following pseudo-first-order kinetics with a rate similar to that observed in the electrochemical experiments ($k_{obs} = 2.99 \times 10^{-4}$ s^{-1} at 217 mM NH_3 at room temperature), as observed by electronic absorption spectra (Fig. 3d) and a colour change from purple to amber. After sparging the resulting $[Ru_2]^{4+}$ solution with N_2 to remove excess NH_3, a stream of O_2 was bubbled through the solution, resulting in fast oxidation (15 min) to the $[Ru_2]^{5+}$ oxidation state as observed by the growth of bands at 522 and 675 nm in the electronic absorption spectra and a characteristic colour change from amber back to purple (Fig. 3e). After another 100 equivalents of NH_3 was added, reduction back to $[Ru_2]^{4+}$ was observed over the course of 2 h (Fig. 3f). This experiment demonstrates that these diruthenium complexes are capable of performing the fundamental chemistry necessary for a DAFC.

Experimental and theoretical mechanistic investigations. In both stoichiometric and electrochemical studies, kinetics experiments suggest a rate-limiting reaction of NH_3 with a $[Ru_2]^{5+}$ species. We provide some critical insights into the mechanism of the transformation shown in equation (4), where the $[Ru_2]^{5+}$ species **2** spontaneously reacts with ammonia to evolve dinitrogen and produce ammonium cation. Given ammonia's dual role as both a reductant and a Brønsted base, we sought to probe the latter function by examining the effect of added NH_4^+ to the reaction of **2** with NH_3. The presence of 20 equivalents of NH_4OTf (with respect to **2**) slowed the reaction by a factor of three (Supplementary Fig. 11

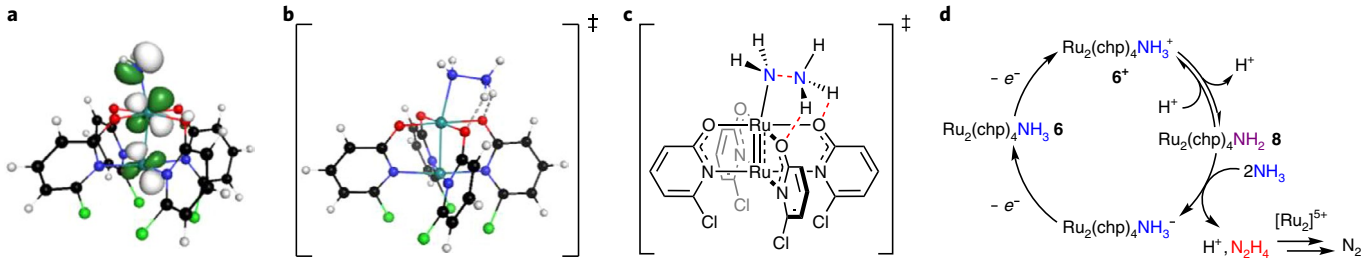

Fig. 5 | Ru_2 electronic structural features and proposed mechanism of ammonia reactivity. a, DFT orbital calculation showing the Ru–Ru–NH_2 π* LUMO in **8**. Analogous orbitals are shown for **9** and **10** in Extended Data Figs. 4 and 5. **b**,**c**, DFT-calculated geometry (**b**) and drawn representation (**c**) of transition state **TS 1** showing the formation of an N–N bond via nucleophilic attack of NH_3 on **8**. Analogous representations of **TS 2** and **TS 3** are shown in Extended Data Figs. 4 and 5. **d**, Proposed catalytic cycle for electrochemical oxidation of ammonia.

and Supplementary Table 16), suggesting a mechanism with at least one deprotonation occurring at or before the rate-determining step. Taken together with the first-order kinetics observed in $[Ru_2]$, we propose the intermediacy of a neutral amido complex $Ru_2(chp)_4NH_2$, **8**, formed upon deprotonation of **3**.

The amido nitrogen atom in **8** possesses a lone pair of π symmetry with respect to the Ru–Ru bond. According to density functional theory (DFT) calculations, complex **8** uses this lone pair in a delocalized, three-centre π interaction extending across the amido nitrogen atom and both ruthenium atoms of the Ru_2 core (Fig. 5a). Calculations suggest that this interaction lifts the degeneracy of Ru–Ru π* orbitals and destabilizes the resulting three-centre Ru–Ru–N amido π* orbital, which becomes the lowest unoccupied molecular orbital (LUMO) for **8** (Supplementary Fig. 19, 20). Corresponding imido and nitrido species (**9** and **10**, respectively), which could form via disproportionation of the parent amido complex **8** (equations (5) and (6)), display analogous three-centre Ru–Ru–N π* interactions (Extended Data Figs. 4 and 5). Much like the empty three-centre Rh–Rh–C carbene π* orbital in Rh_2–carbene species[20,22], this feature confers electrophilic character to the axially bound nitrogen atom of **8**–**10**, thus providing an avenue to N–N bond formation through nucleophilic attack of exogenous ammonia at this site. These three-centre orbital interactions that provide a low-energy pathway for N–N bond formation require the presence of a Ru–Ru bond and are therefore absent in mononuclear Ru complexes.

$$\mathrm{Ru_2(chp)_4NH_2\ (8)} \rightarrow \tfrac{1}{2}\mathrm{Ru_2(chp)_4NH\ (9)} + \tfrac{1}{2}\mathrm{Ru_2(chp)_4NH_3\ (6)}$$
$$(\Delta G, \Delta H) = (-1.8, -1.7\ \mathrm{kcal\ mol^{-1}}) \quad (5)$$

$$\mathrm{Ru_2(chp)_4NH_2\ (8)} \rightarrow \tfrac{1}{3}\mathrm{Ru_2(chp)_4N\ (10)} + \tfrac{2}{3}\mathrm{Ru_2(chp)_4NH_3\ (6)}$$
$$(\Delta G, \Delta H) = (-8.1, -7.2\ \mathrm{kcal\ mol^{-1}}) \quad (6)$$

The disproportionation reactions yielding **9** and **10** are predicted to be thermodynamically favourable, although the energetic barriers for these reactions are unknown and difficult to estimate. Because these transformations are tantamount to hydrogen-atom transfer (HAT) between separate molecules of **8**, the associated transition states are probably bimolecular in nature. As such, the disproportionation steps are incompatible with the observed first-order kinetics in $[Ru_2]$, at least under the reaction conditions used in this study (low $[Ru_2]$ and high $[NH_3]$), leading us to instead favour a mechanism where **8** directly reacts with ammonia without prior disproportionation into more oxidized reactive intermediates.

Calculated transition states **TS 1**–**3** for reactions of **8**–**10** with ammonia were converged from DFT calculations. The sole imaginary vibrational frequency found for **TS 1** is a stretching mode along the red dashed bonds shown in Fig. 5c, clearly indicating N–N bond formation. Transition states following more oxidized species are predicted to occur earlier (that is, at greater N–N distances) and with lower free energy barriers $\Delta G^{\ddagger}$ for N–N bond formation (Table 1). The transition state entropy $\Delta S^{\ddagger}$ for nucleophilic attack of NH_3 only slightly varies across **TS 1**–**3**, while enthalpic contributions to $\Delta G^{\ddagger}$ become increasingly negative in more oxidized species. This is consistent with the greater electrophilic character of the axial nitrogen site in imido and nitrido intermediates.

Table 1 | Thermodynamic parameters of calculated transition states

	TS 1	TS 2	TS 3
$\Delta G^{\ddagger}$ (kcal mol^{-1})	29.1	10.7	6.1
$\Delta H^{\ddagger}$ (kcal mol^{-1})	17.2	−0.5	−4.9
$\Delta S^{\ddagger}$ (cal mol^{-1} K^{-1})	−40	−38	−37

$\Delta G^{\ddagger}$ values are calculated assuming a temperature of 298.15 K.

The relatively slow reaction rates observed in the experimental work are consistent with the larger energetic barrier predicted for N–N bond formation via nucleophilic attack of NH_3 at **8**, although the precise value of $\Delta G^{\ddagger}$ for **TS 1** is probably overestimated by DFT. Specifically, the magnitude of the $\Delta S^{\ddagger}$ component is expected to be overestimated in our model, which does not include explicit hydrogen-bonding to solvent molecules[34].

Interestingly, hydrogen-bonding interactions between equatorial chp ligands and an incoming ammonia molecule (N···O distances of 2.61 and 2.62 Å) are calculated to play a role in facilitating the formation of an intermediate hydrazinium adduct following **TS 1**. Subsequent deprotonation of this intermediate would yield an anionic $[Ru_2(chp)_4NH_2NH_2]^-$ complex, which may release N_2H_4 into solution (Fig. 5d). We therefore decided to test the kinetic competence of N_2H_4 as a potential reaction intermediate.

Upon addition of excess N_2H_4 to **2**, we observe an instant colour change from purple to amber, indicative of rapid reduction from $[Ru_2]^{5+}$ to $[Ru_2]^{4+}$. This observation demonstrates that N_2H_4 does not persist in the presence of $[Ru_2]^{5+}$ during the electrocatalytic oxidation of NH_3 mediated by **2**. Titration of N_2H_4 into a solution of **2** indicates that 1.25 equivalents of N_2H_4 are needed to reduce **2** fully to the $[Ru_2]^{4+}$ oxidation state (Extended Data Fig. 6), which is consistent with N_2H_4 acting as a reductant and as a Brønsted base in the formation of N_2 and a $[Ru_2]^{4+}$ complex (equation (7)). These results indicate that N_2H_4 is kinetically competent to produce N_2 upon

reaction with $[Ru_2]^{5+}$ species, and suggest, but not conclusively establish, its potential role as an intermediate in NH_3 oxidation catalysed by Ru_2 complexes.

$$\begin{aligned} &Ru_2\,(chp)_4\,OTf(2) + \tfrac{5}{4}\,N_2H_4 \\ &\rightarrow Ru_2\,(chp)_4 + \tfrac{1}{4}\,N_2 + N_2H_5OTf \end{aligned} \quad (7)$$

Conclusions

A metal–metal bonded diruthenium complex is capable of performing electrocatalytic oxidation of ammonia at low overpotentials, operating below the thermodynamic potential for the ORR. Moreover, we provide proof-of-concept evidence that the diruthenium AOR catalyst may be regenerated by reaction with molecular oxygen, a finding that is unique among other reported molecular AOR catalysts. Our mechanistic investigations show that the metal–metal multiple bond enables N–N bond formation without the need to access high-energy Ru=NH imido or Ru≡N nitrido species required for monoruthenium systems to perform the AOR[14,15]. This feature is the key that enables facile reoxidation of $[Ru_2]^{4+}$ species with molecular oxygen, opening a door for the exploration of new catalysts with even lower $[Ru_2]^{4+/5+}$ potentials as possible components in direct ammonia fuel cells, an exciting advance towards the realization of a nitrogen economy.

Online content

Any methods, additional references, Nature Research reporting summaries, source data, extended data, supplementary information, acknowledgements, peer review information; details of author contributions and competing interests; and statements of data and code availability are available at https://doi.org/10.1038/s41557-021-00797-w.

Received: 3 December 2019; Accepted: 24 August 2021;
Published online: 8 November 2021

References

1. Elishav, O., Lewin, D. R., Shter, G. E. & Grader, G. S. The nitrogen economy: economic feasibility analysis of nitrogen-based fuels as energy carriers. *Appl. Energy* **185**, 183–188 (2017).
2. Adli, N. M., Zhang, H., Mukherjee, S. & Wu, G. Review—ammonia oxidation electrocatalysis for hydrogen generation and fuel cells. *J. Electrochem. Soc.* **165**, J3130–J3147 (2018).
3. Lan, R., Irvine, J. T. S. & Tao, S. Ammonia and related chemicals as potential indirect hydrogen storage materials. *Int. J. Hydrogen Energy* **37**, 1482–1494 (2012).
4. Chen, J. G. et al. Beyond fossil fuel-driven nitrogen transformations. *Science* **360**, eaar6611 (2018).
5. Zhao, Y. et al. An efficient direct ammonia fuel cell for affordable carbon-neutral transportation. *Joule* **3**, 2472–2484 (2019).
6. Giddey, S., Badwal, S. P. S. & Kulkarni, A. Review of electrochemical ammonia production technologies and materials. *Int. J. Hydrogen Energy* **38**, 14576–14594 (2013).
7. Hansson, J., Brynolf, S., Fridell, E. & Lehtveer, M. The potential role of ammonia as marine fuel—based on energy systems modeling and multi-criteria decision analysis. *Sustainability* **12**, 3265 (2020).
8. Valera-Medina, A., Xiao, H., Owen-Jones, M., David, W. I. F. & Bowen, P. J. Ammonia for power. *Prog. Energy Combust. Sci.* **69**, 63–102 (2018).
9. Wang, D. B. et al. Energy-efficient nitrogen reduction to ammonia at low overpotential in aqueous electrolyte under ambient conditions. *ChemSusChem* **11**, 3416–3422 (2018).
10. Imamura, K. & Kubota, J. Electrochemical membrane cell for NH_3 synthesis from N_2 and H_2O by electrolysis at 200 to 250 °C using a Ru catalyst, hydrogen-permeable Pd membrane and phosphate-based electrolyte. *Sustain. Energy Fuels* **2**, 1278–1286 (2018).
11. Guo, X., Zhu, Y. & Ma, T. Lowering reaction temperature: electrochemical ammonia synthesis by coupling various electrolytes and catalysts. *J. Energy Chem.* **26**, 1107–1116 (2017).
12. Siddharth, K., Chan, Y., Wang, L. & Shao, M. Ammonia electro-oxidation reaction: recent development in mechanistic understanding and electrocatalyst design. *Curr. Opin. Electrochem.* **9**, 151–157 (2018).
13. Afif, A. et al. Ammonia-fed fuel cells: a comprehensive review. *Renew. Sustain. Energy Rev.* **60**, 822–835 (2016).
14. Nakajima, K., Toda, H., Sakata, K. & Nishibayashi, Y. Ruthenium-catalysed oxidative conversion of ammonia into dinitrogen. *Nat. Chem.* **11**, 702–709 (2019).
15. Habibzadeh, F., Miller, S. L., Hamann, T. W. & Smith, M. R. 3rd Homogeneous electrocatalytic oxidation of ammonia to N_2 under mild conditions. *Proc. Natl Acad. Sci. USA* **116**, 2849–2853 (2019).
16. Mahdi, R. B., Christine, G., Jeffery A., B. & Timothy H. W. Chemical and electrocatalytic ammonia oxidation by ferrocene. Preprint at https://doi.org/10.26434/chemrxiv.9729635.v1 (2019).
17. Bhattacharya, P. et al. Catalytic ammonia oxidation to dinitrogen by hydrogen atom abstraction. *Angew. Chem. Int. Ed.* **58**, 11618–11624 (2019).
18. Zott, M. D., Garrido-Barros, P. & Peters, J. C. Electrocatalytic ammonia oxidation mediated by a polypyridyl iron catalyst. *ACS Catal.* **9**, 10101–10108 (2019).
19. Dunn, P. L., Johnson, S. I., Kaminsky, W. & Bullock, R. M. Diversion of catalytic C–N bond formation to catalytic oxidation of NH_3 through modification of the hydrogen atom abstractor. *J. Am. Chem. Soc.* **142**, 3361–3365 (2020).
20. Zott, M. D. & Peters, J. C. Enhanced ammonia oxidation catalysis by a low-spin iron complex featuring cis coordination sites. *J. Am. Chem. Soc.* **143**, 7612–7616 (2021).
21. A. J. Bard, L. R. F. *Electrochemical Methods: Fundamentals and Applications* 2nd edn (John Wiley, 2000).
22. Lindley, B. M., Appel, A. M., Krogh-Jespersen, K., Mayer, J. M. & Miller, A. J. M. Evaluating the thermodynamics of electrocatalytic N_2 reduction in acetonitrile. *ACS Energy Lett.* **1**, 698–704 (2016).
23. Pegis, M. L. et al. Standard reduction potentials for oxygen and carbon dioxide couples in acetonitrile and *N*,*N*-dimethylformamide. *Inorg. Chem.* **54**, 11883–11888 (2015).
24. Coetzee, J. F. & Padmanabhan, G. R. Properties of bases in acetonitrile as solvent. IV. Proton acceptor power and homoconjugation of mono- and diamines. *J. Am. Chem. Soc.* **87**, 5005–5010 (1965).
25. Corcos, A. R., Pap, J. S., Yang, T. & Berry, J. F. A synthetic oxygen atom transfer photocycle from a diruthenium oxyanion complex. *J. Am. Chem. Soc.* **138**, 10032–10040 (2016).
26. Varela-Álvarez, A. et al. Rh_2(II,III) Catalysts with chelating carboxylate and carboxamidate supports: electronic structure and nitrene transfer reactivity. *J. Am. Chem. Soc.* **138**, 2327–2341 (2016).
27. Kornecki, K. P. et al. Direct spectroscopic characterization of a transitory dirhodium donor–acceptor carbene complex. *Science* **342**, 351 (2013).
28. Berry, J. F. The role of three-center/four-electron bonds in superelectrophilic dirhodium carbene and nitrene catalytic intermediates. *Dalton Trans.* **41**, 700–713 (2012).
29. Chakravarty, A. R., Cotton, F. A. & Tocher, D. A. New isomeric form of the '$M_2(OC_5H_3NCl)_4$' core: a polar arrangement of the four 6-chloro-2-hydroxypyridinato (chp) ligands in a chlorodiruthenium(II,III) complex, $Ru_2Cl(chp)_4$. *Inorg. Chem.* **24**, 1263–1267 (1985).
30. Corcos, A. R., Long, A. K. M., Guzei, I. A. & Berry, J. F. A synthetic cycle for nitrogen atom transfer featuring a diruthenium nitride intermediate. *Eur. J. Inorg. Chem.* **2013**, 3808–3811 (2013).
31. Corcos, A. R. & Berry, J. F. Anilinopyridinate-supported Ru_2^{x+} (x = 5 or 6) paddlewheel complexes with labile axial ligands. *Dalton Trans.* **46**, 5532–5539 (2017).
32. Cotton, F. A., Kim, Y. & Yokochi, A. Regioisomerism displayed by the 6-chloro-2-oxopyridinate complexes of Ru_2^{4+} and Ru_2^{5+}. *Inorg. Chim. Acta* **236**, 55–61 (1995).
33. Brown, T. R., Dolinar, B. S., Hillard, E. A., Clérac, R. & Berry, J. F. Electronic structure of Ru_2(II,II) oxypyridinates: synthetic, structural, and theoretical insights into axial ligand binding. *Inorg. Chem.* **54**, 8571–8589 (2015).
34. Besora, M., Vidossich, P., Lledós, A., Ujaque, G. & Maseras, F. Calculation of reaction free energies in solution: a comparison of current approaches. *J. Phys. Chem. A* **122**, 1392–1399 (2018).

Methods

General information. Complex **1** was synthesized according to previously published methods[31]. All other compounds and solvents were obtained and used as received, except when noted. Air-sensitive synthesis was performed under inert gas using Schlenk techniques or in an MBraun Unilab glovebox with a nitrogen atmosphere. Acetonitrile (CH_3CN), DMSO ($(CH_3)_2SO$) and pentane were dried over molecular sieves in a glovebox prior to use. Dichloromethane (CH_2Cl_2) was dried over calcium hydride, distilled under nitrogen and stored in a glovebox over molecular sieves prior to use. All solvents stored over molecular sieves were filtered over celite or through a 0.2 µm syringe filter immediately before use.

NMR spectroscopy, mass spectrometry and X-ray crystallography experiments were performed in the Paul Bender Chemical Instrumentation Center in the Chemistry Department at the University of Wisconsin-Madison. NMR spectra were taken on a Bruker Avance 400 MHz spectrometer. Infrared spectra were taken on a Bruker Tensor 27 Fourier transform infrared (FTIR) spectrometer using an attenuated total reflectance (ATR) adapter. Electronic absorption spectra were obtained using a StellarNet miniature BLUE-wave ultraviolet–visible dip probe with a tungsten–krypton light source and various path length tips. Elemental analyses were measured at Midwest Microlab. Mass spectral data for characterization were collected on a Thermo Scientific Q Exactive Plus mass spectrometer. Mass spectral data for labelled ammonia experiments were collected on a Pfeiffer ThermoStar GSD 320 T3 mass spectrometer when probing the stoichiometric reaction and on an MKS Cirrus2 RGA mass spectrometer when performing Faradaic efficiency measurements under electrocatalytic conditions.

Synthesis and characterization of novel compounds. *$Ru_2(chp)_4OTf$ (**2**).* A Schlenk flask was charged with 340 mg of **1** (0.45 mmol), 240 mg of thallium triflate (0.68 mmol, 1.5 equiv.), a magnetic stir bar and 50 ml of CH_3CN. The reaction mixture was heated to 60 °C overnight. The solvent was then removed under vacuum, heating to 50 °C at the end to ensure dryness. The purple product was extracted into 30 ml of CH_2Cl_2 and filtered over a pad of celite. The flask and filter pad were rinsed with a total of 20 ml of CH_2Cl_2. The combined purple extracts were concentrated under vacuum to a volume of ~5 ml and transferred to a tared vial. Pentane was added until the solution turned cloudy, and the mixture was cooled to −25 °C to crystallize the product. The supernatant was removed via pipette and the purple crystalline product was dried under vacuum (343 mg, 88% yield). ^{1}H-NMR (400 MHz, CH_3CN-d_3) δ, ppm: 33.50 (s, Ar–H, 4H), −24.55 (s, Ar–H, 4H), −68.33 (s, Ar–H, 4H). λ_{max}, nm (ε, $M^{-1}cm^{-1}$): 529 (4,200), 673 (2,900). ATR-FTIR (cm^{-1}): 3,101 (vw), 1,596 (m), 1,535 (m), 1,443 (sh), 1,434 (s), 1,391 (w), 1,343 (m), 1,318 (m), 1,279 (w), 1,262 (w), 1,231 (m), 1,205 (m), 1,175 (m), 1,077 (w), 1,015 (m), 941 (m), 931 (m), 791 (s), 723 (s), 633 (s). Fourier transform mass spectrometry (electrospray ionization): 716.7681; calculated 716.7681 $[Ru_2(chp)_4^+]$; analytical calculated for $C_{21}H_{12}N_4O_7Cl_4Ru_2 \cdot 1.2(CH_2Cl_2)$: C, 27.57; H, 1.50; N, 5.79; found: C, 27.58; H, 1.73; N, 5.99.

$[Ru_2(chp)_4NH_3]OTf$ (3). Compound **2** (29 mg, 0.033 mmol) was dissolved in ~1 ml of CH_3CN and cooled to −25 °C. A −25 °C solution of NH_3 in THF (0.4 M, 84 µl, 1 equiv.) was added and the vial was shaken to mix the solutions. Cold Et_2O was layered above the solution at −25 °C to yield purple crystals (20 mg, 69% yield). Crystals of **3** are semistable at room temperature but decompose in solution. λ_{max} (CH_3CN), nm (ε, $M^{-1}cm^{-1}$): 522 (4,300), 675 (1,900). ATR-FTIR (cm^{-1}): 3,253 (NH, vw), 3,161 (w), 3,108 (vw), 2,979 (vw), 2,878 (vw), 1,610 (sh), 1,596 (m), 1,534 (m), 1,443 (s), 1,435 (sh), 1,390 (w), 1,344 (m), 1,284 (m), 1,258 (s), 1,226 (w), 1,168 (m), 1,103 (w), 1,078 (w), 1,031 (m), 1,016 (m), 931 (m), 879 (vw), 843 (vw), 796 (s), 755 (vw), 755 (w), 722 (s), 636 (s), 607 (w).

*$[Ru_2(chp)_4NH_3(18\text{-}crown\text{-}6)]OTf$ (**4**).* Compound **2** (38 mg, 0.044 mmol) and 18-crown-6 (12 mg, 0.044 mmol) were dissolved in ~1 ml of CH_3CN and cooled to −25 °C. A cold solution of NH_3 in THF (0.4 M, 110 µl, 1 equiv.) was added and the vial was shaken to mix the solutions. Cold Et_2O was layered above the solution at −25 °C to yield purple crystals suitable for X-ray diffraction (30 mg, 60% yield). Crystals of **4** are semistable at room temperature but decompose in solution. ATR-FTIR (cm^{-1}): 3,305 (NH, vw), 3,249 (NH, vw), 3,172 (w), 3,098 (vw), 2,886 (w), 1,596 (m), 1,533 (m), 1,477 (m), 1,441 (sh), 1,435 (s), 1,390 (w), 1,349 (m), 1,268 (m), 1,226 (w), 1,200 (w), 1,160 (m), 1,112 (s), 1,079 (w), 1,059 (w), 1,032 (m), 1,015 (m), 961 (m), 930 (m), 841 (m), 797 (m), 772 (m), 755 (w), 722 (m), 637 (s).

*$Ru_2(chp)_4{-}OS(CH_3)_2$ (**5**).* Synthesis and characterization of **5** has been reported[33] but a modified procedure was used here. A Schlenk flask was charged with **1** (897 mg, 1.19 mmol), zinc dust (781 mg, 11.9 mmol), 20 ml $(CH_3)_2SO$ and 100 ml CH_3CN. The reaction mixture was stirred vigorously at 80 °C for 3 h as the colour changed from purple to brown. The reaction mixture was then cooled to room temperature and filtered through a medium-porosity filter stick into a 500 ml Schlenk tube. The flask and filter pad were rinsed with an additional 20 ml of anhydrous $(CH_3)_2SO$. Degassed water (~300 ml) was then added to the combined extracts. The resulting mixture was then heated to 80 °C for 15 min and cooled slowly. The resulting brown crystals were collected in air, and dried under vacuum (626 mg, 73% yield). This material crystallizes with one molar equivalent of CH_3CN in the crystal lattice. Analysis calculated for $C_{22}H_{18}C_{l4}N_4O_5Ru_2S + C_2H_3N$: C, 34.50; H, 2.53; N, 8.38; found: C, 34.56; H, 2.50; N, 8.40. ^{1}H-NMR (400 MHz, $(CD_3)_2SO$) δ, ppm: 25.46 (s, Ar–H, 4H), 8.57 (s, Ar–H, 4H), 2.77 (broad s, Ar–H, 4H). ATR-FTIR (cm^{-1}): 3,094 (NH, vw), 3,071 (NH, vw), 2,928 (vw), 1,595 (m), 1,531 (m), 1,468 (s), 1,440 (s), 1,392 (m), 1,357 (m), 1,219 (m), 1,170 (m), 1,016 (m), 998 (m), 1595 (m), 954 (w), 929 (m), 853 (w), 782 (s), 729 (m), 713 (m), 627 (w).

*$Ru_2(chp)_4NH_3$ (**6**).* Complex **6** is not isolable as a solid in pure form due to loss of ammonia when isolating solid samples. However, the complex can be generated in solution in an equilibrium with $Ru_2(chp)_4$–solvent adducts by dissolving complex **5** in ammonia-containing solutions of CH_3CN, $(CH_3)_2SO$ or THF. In a typical preparation, complex **5** (31 mg, 0.043 mmol) was stirred in a 1.05 M NH_3/CH_3CN solution (5.7 ml, ~200 equiv.) for ~10 min before filtering the amber solution through celite, yielding a solution of **6** and **5′** in 1.05 M NH_3/CH_3CN. A similar process was used to make a solution of **6** and **5** in $(CD_3)_2SO$ containing 0.49 M NH_3 for ^{1}H-NMR characterization. ^{1}H-NMR (400 MHz, $(CD_3)_2SO$) δ, ppm: 25.79 (s, Ar–H, 4H), 9.00 (s, Ar–H, 4H), 3.38 (broad s, Ar–H, 4H), 0.58 (broad s, excess NH_3 mixing with $[Ru_2]NH_3$). Cyclic voltammetry measurements discussed in the Supplementary Information (Supplementary Fig. 14) indicate an equilibrium between ammonia and solvent adducts. This is consistent with our observation that the position of the NH signal in ^{1}H-NMR spectra is highly dependent on solvent identity and ammonia concentration. λ_{max} (CH_3CN), nm (ε, $M^{-1}cm^{-1}$): 806 (70).

From a solution of **6** and $Ru_2(chp)_4(THF)$ generated from **5** in THF with 2.2 molar equivalents of NH_3, a solid material was precipitated with pentane and characterized using ATR-FTIR (cm^{-1}): ~3,300 (NH, vw), ~3,250 (NH, vw), 3,169 (w), 1,603 (m), 1,531 (m), 1,465 (s), 1,438 (s), 1,392 (m), 1,357 (m), 1,219 (m), 1,167 (m), 1,074 (w), 1,015 (m), 929 (m), 852 (w), 780 (s), 782 (m), 713 (m).

Crystals of **6** were obtained by diffusion of hexanes into an NH_3/THF solution. Unit cell dimensions $a = b = 19.9253(5)$ Å, $c = 61.4002(17)$ Å, $\alpha = \beta = \gamma = 90°$ (cell volume = 24,377.0(11) Å^3; $Z = 32$). Due to poor data quality, complete refinement was not possible. However, refinement in the tetragonal *P4/nnc* space group yielded a chemically reasonable solution indicating the empirical formula of **6**.

*$[Ru_2(chp)_4NH_3]_2(18\text{-}crown\text{-}6)$ (**7**).* Compound **5** (17 mg, 0.024 mmol) was stirred in 0.4 M NH_3 solution in THF (~1 ml, 15–20 equiv.) for 30 min. The mixture was filtered and 18-crown-6 was added (32 mg, 5 equiv.) to the filtrate and stirred until dissolved. The resulting solution was allowed to sit without stirring. The product crystallizes from solution as amber crystals suitable for X-ray diffraction (17 mg, 73%). ATR-FTIR (cm^{-1}): ~3,330 (NH, vw), ~3,260 (NH, vw), 3,189 (w), 3,096 (vw), 2,918 (w), 1,603 (m), 1,530 (w), 1,468 (m), 1,439 (m), 1,392 (w), 1,351 (m), 1,288 (m), 1,241 (m), 1,222 (m), 1,166 (m), 1,135 (w), 1,099 (s), 1,026 (m), 958 (m), 928 (m), 835 (m), 781 (m), 755 (w), 728 (w), 713 (w), 638 (w). Complex **7** was also isolated from mixtures resulting from reaction of **2** with NH_3 in CH_3CN by adding excess 18-crown-6 and allowing **7** to crystallize from solution; however, it is difficult to obtain pure samples of **7** this way due to the other compounds present in the mixture.

Ammonia solutions. *NH3/CH3CN solutions.* Anhydrous ammonia was bubbled through a solution of CH_3CN for 10–20 min. The flask was then sealed with a Teflon screwcap for storage. The solutions warm as the ammonia dissolves and typically reach a concentration in the 600–700 mM range. If the flask is placed in a room-temperature or cool water bath during addition of ammonia, concentrations above 1 M can be achieved, but these solutions will lose ammonia more quickly when opened at room temperature and the ammonia concentration should be quantified more often.

NH_3/CH_3CN-d_3 solutions. The above procedure was followed except that CH_3CN-d_3 was used instead of CH_3CN.

$^{15}NH_3/CH_3CN$ solutions. A 250 ml Schlenck flask was connected via a T-joint to both an argon Schlenk manifold and a lecture bottle of anhydrous $^{15}NH_3$. The flask was filled with 100 ml freshly distilled acetonitrile and degassed by five freeze–pump–thaw cycles. The degassed solvent in the flask was then frozen solid in liquid nitrogen and placed under static vacuum. The lecture bottle and the stopcock on the Schlenck flask were opened to allow the ammonia gas to flow from the lecture bottle into the evacuated flask and deposit (as a solid) in the frozen flask over 30 min. The stopcock was then closed, and the sealed Schlenck flask was removed from the liquid nitrogen and allowed to warm to room temperature under static vacuum. The flask was then adjusted to atmospheric pressure by briefly opening the side arm of the flask to an argon flow. The solution was allowed to equilibrate in the sealed flask overnight. The concentration of $^{15}NH_3$ was measured using the indophenol method described below.

Quantification of NH_3 in solution. Ammonia concentrations were determined by adaptation of a known procedure[35]. Solution A was prepared with 25 g phenol and 125 mg sodium nitroprusside in 500 ml water (>18 MΩ). Solution B was prepared with 13 g sodium hydroxide and 13 ml of household bleach (8.25%) in

500 ml water. Solutions A and B were stored at 4 °C for no longer than one month. For each analysis, performed five times, 10 ml of solution A was added to a test tube, followed by either 25 µl (for expected concentrations <700 mM) or 10 µl (for expected concentrations >700 mM) of NH_3/CH_3CN solution via a gas-tight syringe. Then 10 ml of solution B was added and the tubes were placed in a warm water bath at 40 °C for 20 min. The solutions were then diluted to 50 ml in a volumetric flask with water. The resulting blue indophenol solutions were analysed by electronic absorption spectroscopy. The average absorbance at 633 nm was used to calculate the concentration of ammonia using a linear relationship established by a set of standard solutions of ammonia in water.

Electrochemical experiments. Electrochemical experiments were performed using a BioLogic SP-200 potentiostat in dry, degassed CH_3CN containing 0.1 M NBu_4PF_6 (tetrabutylammonium hexafluorophosphate, Aldrich, 98%, recrystallized) as the supporting electrolyte. A glassy carbon disk (3 mm diameter, CH Instruments) and a platinum wire were respectively used as the working electrode and the counterelectrode in cyclic voltammetry experiments. The glassy carbon working electrode was polished with an alumina and water slurry, rinsed with methanol and dried between experiments. An RVC block (1.5 × 1.0 × 0.5 cm, 80 PPI, Selee) and 1-mm-diameter platinum rod were respectively used as the working electrode and the counterelectrodes in bulk electrolysis experiments. A fresh block of RVC was cut to identical dimensions for each bulk electrolysis to prevent electrode fouling between experiments. All working electrode potentials were measured versus a $Ag/AgNO_3$ reference electrode (Pine Research) containing an internal solution of 100 mM Bu_4NPF_6 and 10 mM $AgNO_3$ in CH_3CN. The Ag electrode was lightly polished with 600 grit sandpaper between trials to remove any surface corrosion. Solid ferrocene was dissolved in analyte solution at the end of each cyclic voltammetry experiment to provide an internal reference for calibrating potentials to the $Fc^{0/+}$ redox couple in CH_3CN.

CCC experiments were performed in a custom-made bulk electrolysis cell (Extended Data Fig. 2) equipped with a Schlenk side arm and five ports to accommodate an insertable counterelectrode chamber (separated from the working electrode chamber by a 10-mm-diameter fine frit), a dip probe for electronic absorption spectroscopy and detachable electrodes for performing voltammetry and bulk electrolysis measurements. To probe electrocatalytic behaviour, the electrolysis cell was charged with 50 ml of a stock solution containing 0.33 mM **5**, 150 mM Bu_4NPF_6 and 5 mM NH_3 in CH_3CN, and 25 ml of a 705 mM NH_3 solution in CH_3CN. In a stoichiometric electrolysis experiment, 50 ml of this stock solution was instead mixed with 25 ml of CH_3CN.

The cell was placed under N_2 via the Schlenk side arm while a dip-probe and $Ag/AgNO_3$ reference electrode were installed through ports entering the working electrode chamber, and the counterelectrode chamber was charged with 1.3 ml of an 80 mM $FcPF_6$, 100 mM Bu_4NPF_6 solution in CH_3CN. $FcPF_6$ was used as a sacrificial oxidant to balance charge passed at the counterelectrode with charge passed at the working electrode from the bulk oxidation. Electrolysis was performed at +0.5 mA for 145 min while the solution in the working electrode chamber was vigorously stirred to ensure steady-state conditions. Electronic absorbance spectra were collected at 1 min intervals (Supplementary Fig. 12).

CPC experiments for determining Faradic efficiency were performed in a custom-made bulk electrolysis cell consisting of a single chamber assembled by clamping two glass components together around an O-ring (Fig. 4a). To probe electrocatalytic behaviour, a Schlenk flask was charged with **2** (9.0 mg, 0.010 mmol), Bu_4NPF_6 (0.3883 g, 1.002 mmol) and $^{15}NH_3/CH_3CN$ solution (10.0 ml, 0.64 M $^{15}NH_3$). After stirring for 4 h to ensure complete reduction to the $[Ru_2]^{4+}$ redox state, 8.0 ml of the resulting solution was transferred to the electrolysis cell (Fig. 4a) under an argon atmosphere via a syringe. In a control experiment where **2** was absent, an otherwise identical procedure was performed using only Bu_4NPF_6 (0.3872 g, 0.9994 mmol) and $^{15}NH_3/CH_3CN$ solution (10.0 ml, 0.64 M $^{15}NH_3$).

For each experiment, a modified septum was prepared in advance such that wiring connecting electrodes to the potentiostat was run through it and sealed in place with epoxy. The modified septum was then fitted over the top glass component of the electrolysis cell and secured with Teflon tape. A constant potential of 0.00 V versus $Fc^{0/+}$ was applied at the working electrode for 30 min with stirring and then halted for 60 min afterwards. This cycle was performed three times for a total experiment runtime of 270 min and a total electrolysis time of 90 min. At 30 min intervals, 500 µl of reaction headspace was sampled for analysis of $^{15}N^{15}N$ via syringe and slowly injected into a stainless-steel tube passing a constant flow of argon (20 ml min^{-1}) over a capillary inlet to the mass spectrometer. The $^{15}N^{15}N$ produced was quantified by calibrated mass spectrometry as described in the Supplementary Information.

Computational methods. All calculations were performed using version 4.0.0.2 of the ORCA software package[36]. Calculations were performed by unrestricted Kohn–Sham DFT using the B3LYP hybrid functional with D3 dispersion corrections and the RIJCOSX chain-of-spheres approximation[37–40]. A TZVP basis set was used for ruthenium and a def2-SVP basis set was used for all other atoms[41]. Relativistic effects were treated using the zero-order relativistic approximation (ZORA) Hamiltonian with the SARC/J auxiliary basis set for Coulomb fitting[42–48]. The conductor-like polarizable continuum model (CPCM) was implemented to model the solvent effects of acetonitrile[49]. In DFT-optimized geometries for the proposed intermediate structures **6**, $\mathbf{6}^+$, **8**, **9** and **10**, the absence of vibrational modes with imaginary frequency values confirmed that these calculations converged to energetic local minima. In DFT-optimized geometries for the proposed transition states **TS 1–3**, the existence of a single vibrational mode (depicting N–N bond formation) with an imaginary frequency value confirmed that each of these calculations converged to an energetic saddle point. Cartesian coordinates of stationary points are given in Supplementary Tables 19–26. Three-dimensional models of DFT-calculated structures and orbital maps were created using PyMOL[50].

Data availability

Crystallographic data for the structures reported in this article have been deposited at the Cambridge Crystallographic Data Centre, under deposition numbers CCDC 1945089 (**7**), 1945090 (**2**), 1945091 (**4**), 1945092 (**3**) and 2006690 (**5**). Copies of the data can be obtained free of charge via https://www.ccdc.cam.ac.uk/structures/. Source data for Figs. 3 and 4 and Extended Data Fig. 6 are provided with the article. Source data for Extended Data Fig. 1 can be found at https://figshare.com/articles/dataset/Berry_ED_Fig1_mnova/15060798. All other data supporting the findings of this study are available within the article and its Supplementary Information, or from the corresponding author upon reasonable request.

References

35. Weatherburn, M. W. Phenol–hypochlorite reaction for determination of ammonia. *Anal. Chem.* **39**, 971–974 (1967).
36. Neese, F. ORCA, an ab initio, density functional and semi-empirical program package, v.4.0.0.2 (Max Planck Institute for Chemical Energy Conversion, 2018).
37. Neese, F., Wennmohs, F., Hansen, A. & Becker, U. Efficient, approximate and parallel Hartree–Fock and hybrid DFT calculations. A 'chain-of-spheres' algorithm for the Hartree–Fock exchange. *Chem. Phys.* **356**, 98–109 (2009).
38. Grimme, S., Antony, J., Ehrlich, S. & Krieg, H. A consistent and accurate ab initio parametrization of density functional dispersion correction (DFT-D) for the 94 elements H–Pu. *J. Chem. Phys.* **132**, 154104 (2010).
39. Becke, A. D. Density-functional thermochemistry. III. The role of exact exchange. *J. Chem. Phys.* **98**, 5648–5652 (1993).
40. Lee, C., Yang, W. & Parr, R. G. Development of the Colle–Salvetti correlation-energy formula into a functional of the electron density. *Phys. Rev. B* **37**, 785–789 (1988).
41. Weigend, F. & Ahlrichs, R. Balanced basis sets of split valence, triple zeta valence and quadruple zeta valence quality for H to Rn: design and assessment of accuracy. *Phys. Chem. Chem. Phys.* **7**, 3297–3305 (2005).
42. Aravena, D., Neese, F. & Pantazis, D. A. Improved segmented all-electron relativistically contracted basis sets for the lanthanides. *J. Chem. Theory Comput.* **12**, 1148–1156 (2016).
43. Lenthe, E. V., Baerends, E. J. & Snijders, J. G. Relativistic regular two-component Hamiltonians. *J. Chem. Phys.* **99**, 4597–4610 (1993).
44. Pantazis, D. A., Chen, X.-Y., Landis, C. R. & Neese, F. All-electron scalar relativistic basis sets for third-row transition metal atoms. *J. Chem. Theory Comput.* **4**, 908–919 (2008).
45. Bühl, M., Reimann, C., Pantazis, D. A., Bredow, T. & Neese, F. Geometries of third-row transition-metal complexes from density-functional theory. *J. Chem. Theory Comput.* **4**, 1449–1459 (2008).
46. Pantazis, D. A. & Neese, F. All-electron scalar relativistic basis sets for the lanthanides. *J. Chem. Theory Comput.* **5**, 2229–2238 (2009).
47. Pantazis, D. A. & Neese, F. All-electron scalar relativistic basis sets for the actinides. *J. Chem. Theory Comput.* **7**, 677–684 (2011).
48. Pantazis, D. A. & Neese, F. All-electron scalar relativistic basis sets for the 6*p* elements. *Theor. Chem. Acc.* **131**, 1292 (2012).
49. York, D. M. & Karplus, M. A smooth solvation potential based on the conductor-like screening model. *J. Phys. Chem. A* **103**, 11060–11079 (1999).
50. PyMOL molecular graphics system, v.2.5.1 (Schrödinger, 2021).

Acknowledgements

We thank the Department of Energy for funding (DE-SC0021021). We also thank S.-C. Wang in the Hermans group as well as E. Canales and K. Rivera-Dones in the Huber group at UW-Madison for help with the mass spectrometry measurements of labelled nitrogen. We thank M. Aristov and A. Wheaton for assistance with crystallographic data. Crystallographic data were collected on a Cu Kα instrument that was funded by the NSF (CHE-1919350) and on a Mo Kα instrument funded by a generous gift from Paul and Margaret Bender.

Author contributions

M.J.T. performed all electrochemical and spectroelectrochemical experiments and conducted the computational modelling. C.M.W. performed all synthesis and non-crystallographic characterization of diruthenium complexes, preparation

of ammonia solutions, ammonia reactivity experiments and other spectroscopic experiments. T.R.B. performed preliminary synthesis and characterization on diruthenium ammine complexes that directly informed this work. S.V.P. performed crystallographic characterization of the diruthenium compounds. M.J.T., C.M.W. and J.F.B. wrote the manuscript. All authors provided feedback during the manuscript preparation and approved the final manuscript.

Competing interests

M.J.T., C.M.W., T.R.B., S.V.P. and J.F.B. have submitted a provisional patent application based on the work described here (US patent application number P200013US01).

Additional information

Extended data are available for this paper at https://doi.org/10.1038/s41557-021-00797-w.

Supplementary information The online version contains supplementary material available at https://doi.org/10.1038/s41557-021-00797-w.

Correspondence and requests for materials should be addressed to John F. Berry.

Peer review information *Nature Chemistry* thanks Dai Oyama and the other, anonymous, reviewer(s) for their contribution to the peer review of this work.

Reprints and permissions information is available at www.nature.com/reprints.

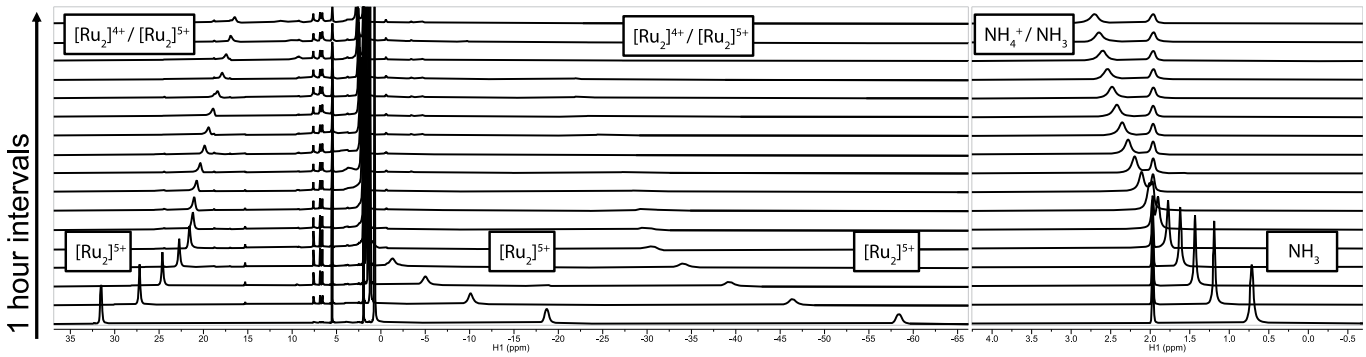

Extended Data Fig. 1 | ^{1}H-NMR spectra monitoring the reaction of 2 with ammonia in CH_3CN-d_3. Left: Portion of spectra focused on the Ar-H signals in the diruthenium complex. Right: Portion of spectra focused on the NH_3/NH_4^+ signal shifting over the course of the experiment. Spectra are collected at 1-hour intervals.

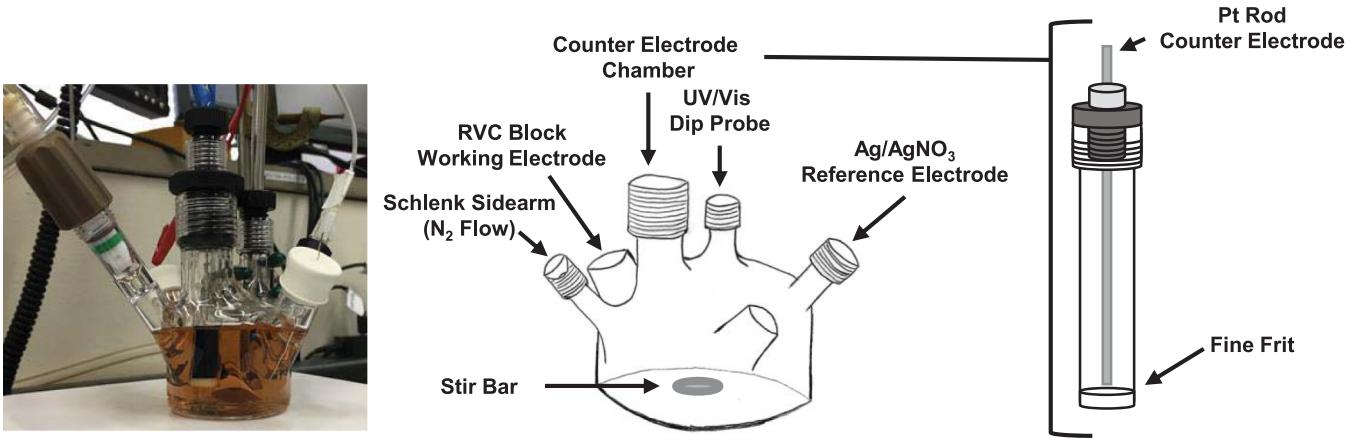

Extended Data Fig. 2 | Spectroelectrochemical cell used in controlled current Coulometry experiments. Left: A photograph of the spectroelectrochemical cell, loaded with a solution of **5** with excess ammonia in the working electrode chamber and a solution of $FcPF_6$ sacrificial oxidant in the counter electrode chamber. Right: A schematic of the spectroelectrochemical cell detailing its assembly.

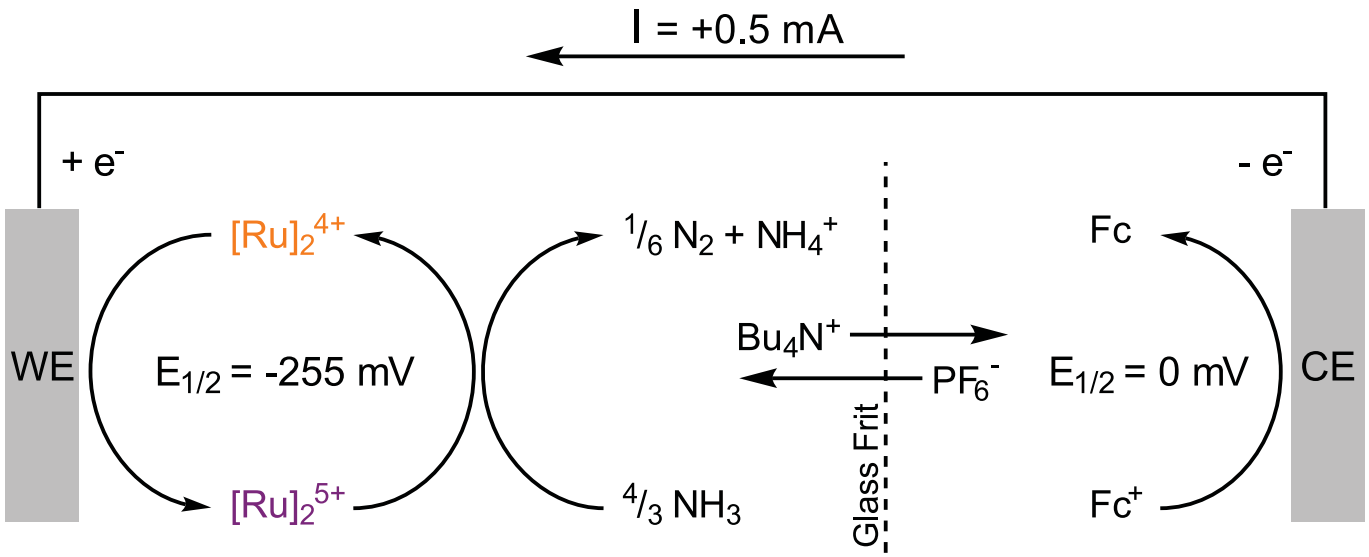

Extended Data Fig. 3 | Electrode and chemical processes occurring during controlled current Coulometry. Diruthenium species in the $[Ru_2]^{4+}$ oxidation state are electrochemically oxidized to the $[Ru_2]^{5+}$ oxidation state at the surface of the reticulated vitreous carbon (RVC) working electrode (WE). The redox potential for this transformation is −255 mV vs $Fc^{0/+}$ in CH_3CN. Applied potential at WE is adjusted throughout the experiment to maintain a constant oxidizing current of +0.5 mA. Exogenous ammonia in solution spontaneously reacts with $[Ru_2]^{5+}$ species to produce dinitrogen and ammonium while regenerating $[Ru_2]^{4+}$ species. The ferrocenium cation in $FcPF_6$ is electrochemically reduced to neutral ferrocene at the surface of the platinum counter electrode (CE). The working electrode and counter electrode chambers are divided by a fine glass frit allowing for ion exchange.

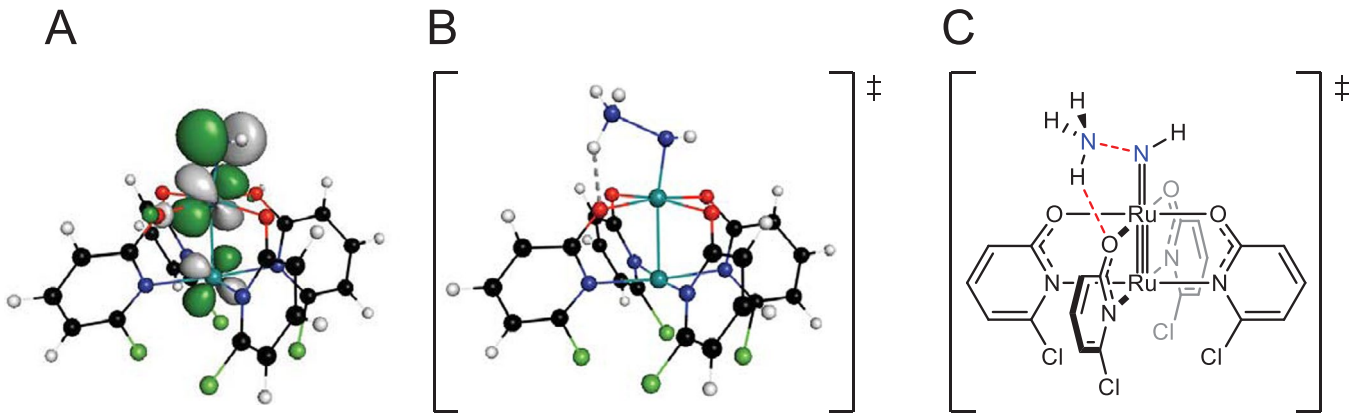

Extended Data Fig. 4 | Electronic structural features and proposed mechanism of ammonia reactivity with an imido intermediate. A: DFT orbital calculation showing the Ru-Ru-NH π^* LUMO in **9**. **B**,**C**: DFT-calculated geometry (**B**) and drawn representation (**C**) of transition state **TS2** showing the formation of an N-N bond via nucleophilic attack of NH_3 on **9**.

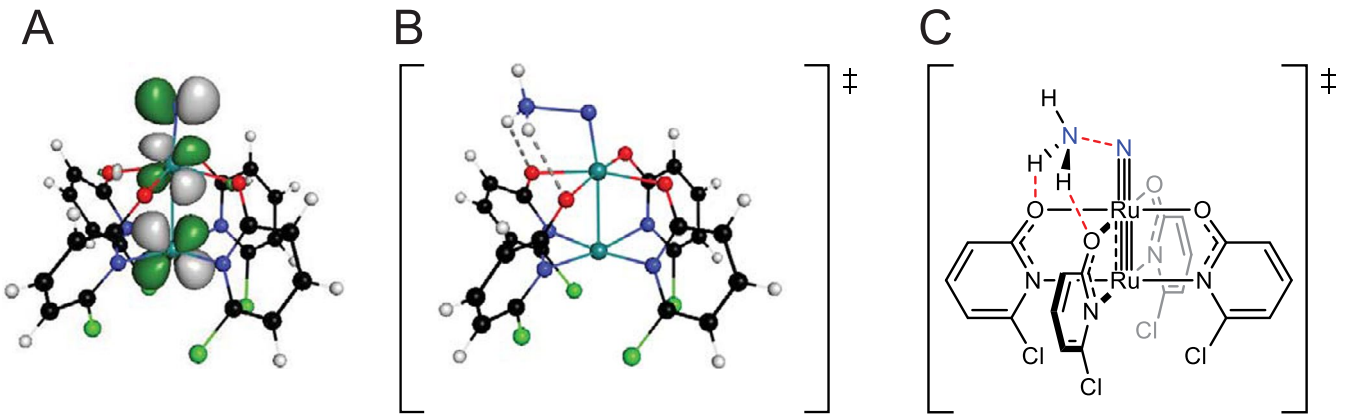

Extended Data Fig. 5 | Electronic structural features and proposed mechanism of ammonia reactivity with a nitrido intermediate. A: DFT orbital calculation showing the Ru-Ru-N π^* LUMO in **10**. **B**,**C**: DFT-calculated geometry (**B**) and drawn representation (**C**) of transition state **TS3** showing the formation of an N-N bond via nucleophilic attack of NH_3 on **10**.

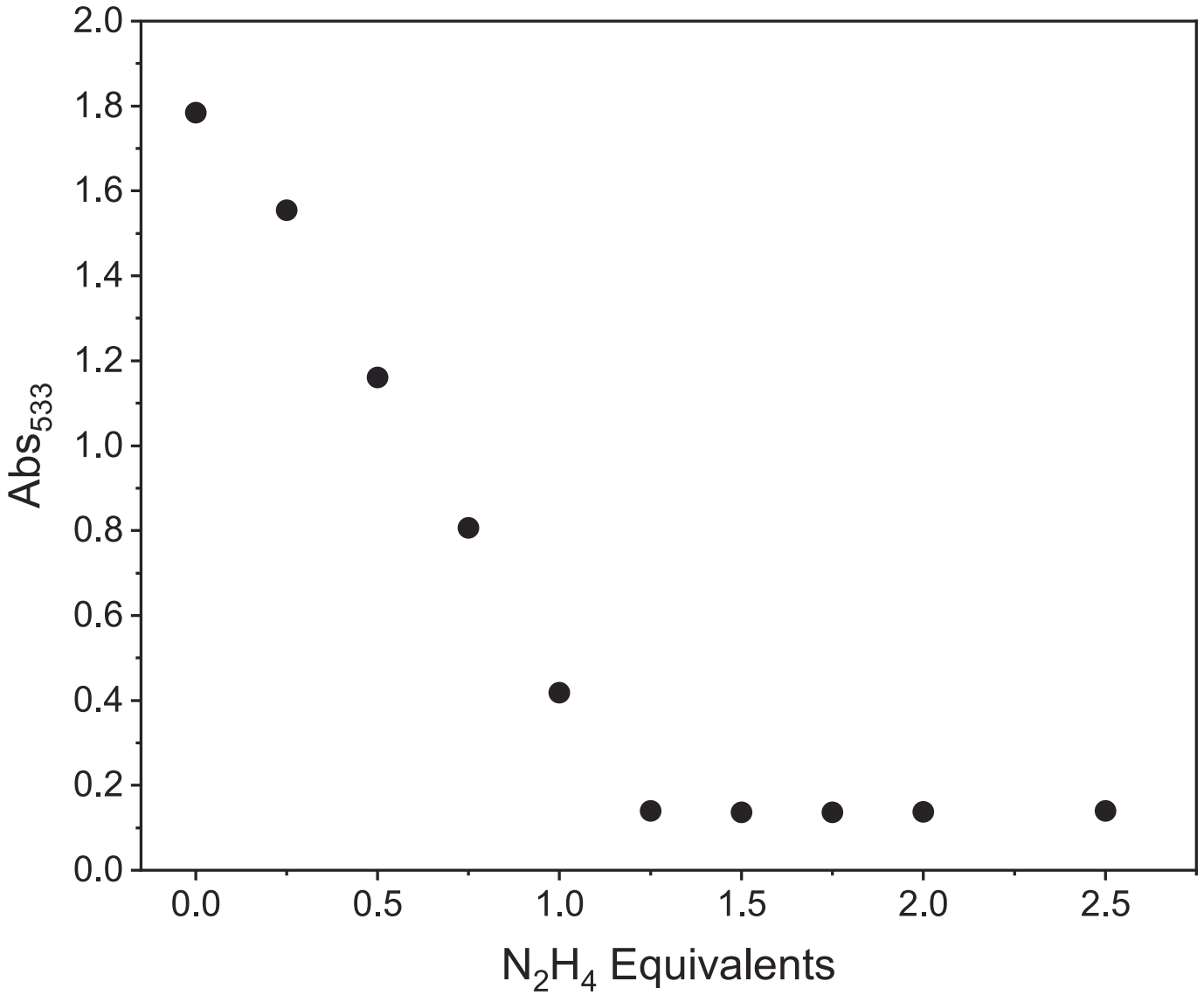

Extended Data Fig. 6 | Titration of 2 with N_2H_4 in CH_3CN monitored by electronic absorption spectroscopy. The trace of absorbance at 533 nm versus equivalents of N_2H_4 shows a distinct end to the reaction after the addition 1.25 equivalents.